Experimental Comparison of Classical versus Ablative Rayleigh-Taylor Instability

K. S. Budil, B. A. Remington, T. A. Peyser, K. O. Mikaelian, P. L. Miller, N. C. Woolsey,
W. M. Wood-Vasey,* and A. M. Rubenchik

Lawrence Livermore National Laboratory, Livermore, California 94550

(Received 26 February 1996)

The evolution of the Rayleigh-Taylor instability in a compressible medium has been investigated both at an accelerating embedded interface and at the ablation front in experiments on the Nova laser. Planar targets of brominated plastic for the ablation front and brominated plastic backed by a titanium payload for the embedded interface were ablatively accelerated by the x-ray drive generated in a gold *Hohlraum.* When the perturbation is at the ablation front, short wavelength modes are stabilized, whereas at the embedded interface the shortest wavelengths grow the most. [S0031-9007(96)00348-1]

PACS numbers: 52.35.Py, 47.40.Nm, 52.50.Jm, 52.70.La

The Rayleigh-Taylor (RT) instability [1] occurs when a lower density fluid accelerates a higher density fluid. This interface instability, also known as the fluid interchange instability, causes "spikes" of the higher density fluid to penetrate down through the lower density fluid and "bubbles" of the latter to rise through the heavier layer. Nature is replete with examples of the RT instability and its shock analog, the Richtmyer-Meshkov (RM) [2] instability. A recent example from astrophysics is the occurrence of strong RT-driven mix in the evolution of Supernova 1987A [3]. Another area where the RT instability occurs is in inertial confinement fusion (ICF) [4, 5]. When a capsule is ablatively imploded, the ablation front is RT unstable during the acceleration phase and the pusher-fuel interface is RT unstable during the deceleration and stagnation phase. Strong perturbation growth can lead to spikes of the capsule wall material protruding into the fuel, which can severely degrade capsule performance [6].

In ICF, a clear distinction has been drawn between classical and ablative RT evolution, the latter widely believed to exhibit reduced growth compared to classical due to the stabilization effects from ablation and density gradients. Theoretical and numerical investigations of the ablative RT instability are numerous, and differ considerably on the level of stabilization expected [4–8]. Previous experimental investigations of ablation-front RT growth have typically compared measurements with predicted classical growth based on numerical simulations [9, 10]. We present here the first direct experimental observation of the stabilization of RT growth at an ablation front by comparing with measured growth at an embedded RT-unstable interface under nearly identical conditions.

The experimental configuration is shown in Fig. 1 and is described in more detail elsewhere [10, 11]. A 750 μm diameter planar package is mounted across a hole on a 3 mm long, 1.6 mm diameter gold cylindrical *Hohlraum*. Eight of the 10 Nova laser beams at a wavelength of 0.351 μm are used to generate a 3.3 ns low-adiabat, shaped drive, as shown in Fig. 2(a). Two 3 ns temporally square beams at a wavelength of 0.528 μm are delayed by 2 ns relative to the start of the drive lasers and focused onto either an iron (for the embedded interface experiments) or molybdenum (for the ablation-front experiments) backlighter disk to generate hard x rays to back-illuminate the accelerating planar foil. The Fe backlighter spectrum is dominated by 6.7 keV He-α x rays, and the Mo spectrum is dominated by a broad L band centered at 2.6 keV. Random phase plates with 5 mm diameter hexagonal elements are inserted as the last optic in the two backlighter lasers to generate a smooth 700 μm diameter x-ray spot. For each experiment, two-dimensional gated x-ray images were obtained with a recently developed gated x-ray pinhole camera [12]. Four gated pinhole images are obtained for each of the four strips on the microchannel plate detector.

The *Hohlraum* radiation drive was extensively characterized previously [10, 11], and was checked here with

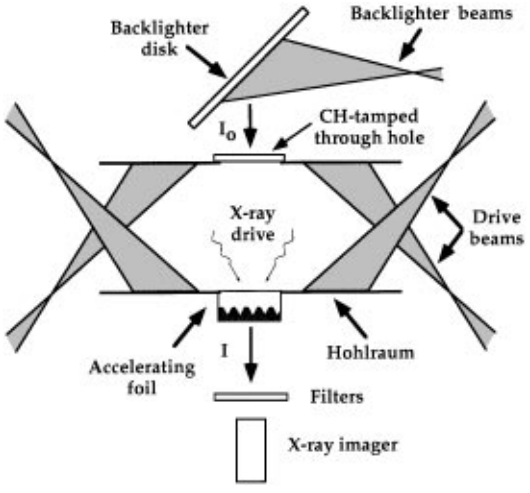

FIG. 1. Experimental configuration for RT experiments. The accelerating foil shown is for the embedded interface experiments which consists of a 35 μm thick CH(Br) ablator (white) backed by a 15 μm thick Ti payload (dark gray).

 0031-9007/96/76(24)/4536(4)$10.00

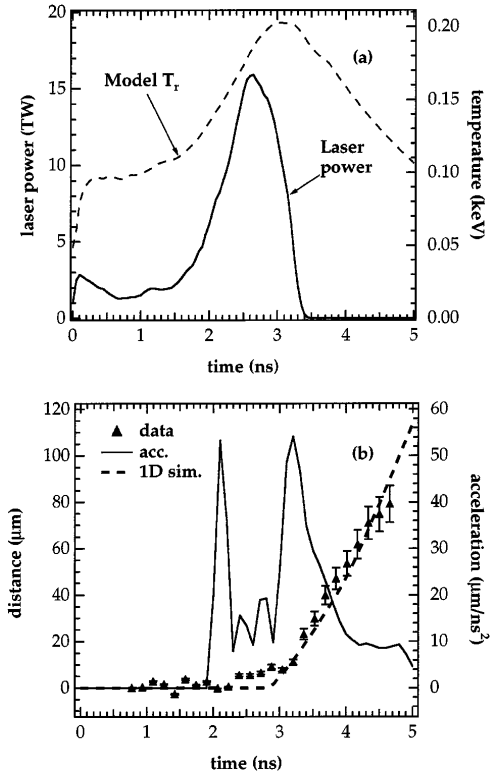

FIG. 2. (a) Typical total laser power, and corresponding radiation drive temperature history. (b) The corresponding trajectory for the back edge of the foil (experimental and 1D simulation) for the drive shown in (a), and the deduced interface acceleration profile, based on 1D radiation-hydrodynamics simulations for the embedded interface.

foil trajectory measurements with the CH(Br)-Ti composite foils, as shown in Fig. 2(b). The foil does not move as a unit until the shock breaks out the back side of the Ti at $t = 2.9$ ns. The trajectory results for the ablation-front foils can be found in Refs. [10, 11]. The perturbation growth data were taken at $t \geq 2.7$ ns, to focus on the RT evolution of the foil, as opposed to the foil dynamics during shock transit.

Two types of target were investigated. The classical, or embedded interface targets consisted of a 35 μm thick CH(Br) ablator ($C_{50}H_{47}Br_3$, $\rho = 1.26$ g/cm^3) backed by a 15 μm thick Ti payload ($\rho = 4.5$ g/cm^3). Sinusoidal ripples were machined at the CH(Br)-Ti interface corresponding to (on separate targets) wavelengths of $\lambda = 10$, 20, 50, and 100 μm and amplitudes of $\eta_0 = 0.5$ and 1.0 μm. The targets were made by machining the sinusoidal grooves into copper disks, which were then sputter coated with Ti, whose back side was polished flat. The Cu mandrel was acid etched away, and then the 35 μm layer of CH(Br) was hot pressed onto the rippled Ti surface. The ablation front experiments used thicker (50–60 μm) CH(Br) foils with no Ti payload, and had the ripples molded onto the ablation-front side. In both cases, the perturbations, characterized by atomic

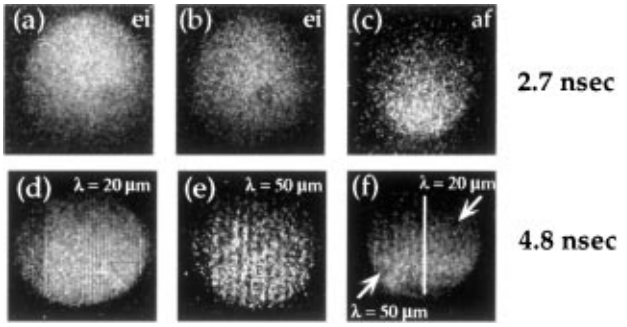

FIG. 3. Images of the raw film density data. (a) Image of the $\lambda = 20$ μm perturbation, embedded interface foil at 2.7 ns. (b) Same, only for the $\lambda = 50$ μm perturbation. (c) Same, only for the ablation-front foil with $\lambda = 20$ μm side by side with $\lambda = 50$ μm on the same foil. (d)–(f) The same perturbations ($\lambda = 20$ μm, $\lambda = 50$ μm, and $\lambda = 20 + 50$ μm side by side) at $t = 4.8$ ns.

force microscopy and contact profilometry, are known to better than 10%.

In Fig. 3 we show sample experimental images from the "raw" data. Across the top row are images taken early in time, at 2.7 ns, of (a) the $\lambda = 20$ μm perturbation and (b) the $\lambda = 50$ μm perturbation both at the embedded interface of the composite targets, and (c) a side-by-side $\lambda = 20$ and 50 μm perturbation at the ablation front of a single CH(Br) foil. Figures 3(d)–3(f) show images from the same accelerated foils later in time (4.8 ns). The present measurements confirm previous ablation-front results at $\lambda = 50$ μm [11] and extend the ablation-front data set to $\lambda = 20$ μm. The perturbation initial amplitudes were $\eta_0 = 1$ μm for the $\lambda = 20$, 50, and 100 μm perturbations at the embedded interface and $\eta_0 = 0.5$ μm for $\lambda = 10$ μm at the embedded interface (not shown) as well as for $\lambda = 20$ and 50 μm at the ablation front.

To quantify the results shown in Fig. 3, we Fourier analyze the ln(exposure) $= -\int \rho\kappa\, dz$ of the images, where ρ is density and κ is opacity. We present in Fig. 4 the growth of the fundamental mode versus time, normalized to its value at $t = 0$. In this growth factor representation, the effect of the instrument spatial resolution largely divides out. The $\lambda = 10$ μm perturbation exhibits the highest growth factor, 22, compared to peak growth factors of approximately 12.5, 3.5, and ≤ 1.5 for wavelengths of 20, 50, and 100 μm, respectively. Figure 4(b) shows the ablation-front measurements, where the peak growth factors were ~ 17 for $\lambda = 50$ μm perturbation and ~ 1 (i.e., no growth) for the $\lambda = 20$ μm ripple. For the embedded interface, the growth at $\lambda = 20$ μm is a factor of ~ 3–4 *higher* than that at $\lambda = 50$ μm at the same time, whereas for the ablation-front experiment, the growth at $\lambda = 20$ μm is over a factor of ~ 10 *less* than that observed for $\lambda = 50$ μm. Note that the diagnostic and x-ray drives were identical throughout these measurements.

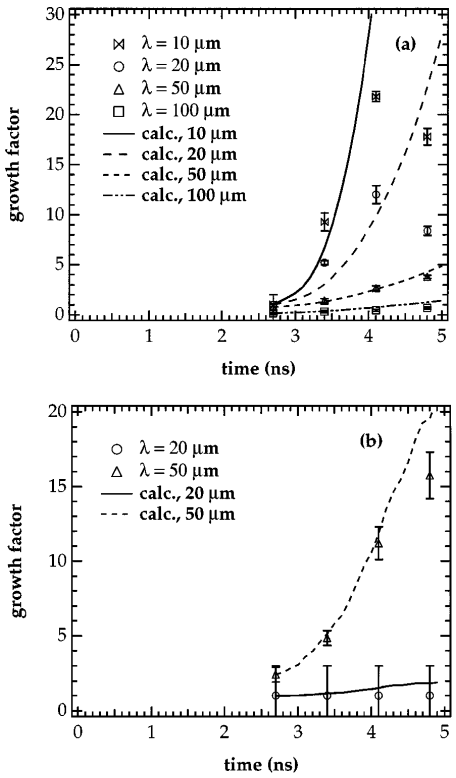

FIG. 4. (a) Growth factor of the fundamental mode of contrast vs time for the $\lambda = 10$, 20, 50, and 100 μm perturbation at the embedded interface. (b) Same, only for growth at the ablation front. The curves in (a) correspond to the result of a classical RT growth calculation, and in (b) to a calculation with the Takabe relation.

The higher overall growth for $\lambda = 50$ μm at the ablation front compared to the embedded interface is due to two factors. The peak acceleration for the CH(Br) foil is a factor of 2 higher due to its lower mass and the period of exponential RT growth is longer due to the earlier breakout of the shock ($t = 2.6$ ns).

The experimental results for the embedded interface are compared with classical theory, using the 1D radiation-hydrodynamics code HYADES [13] to generate the gross foil hydrodynamics. The 1D simulations, using the *Hohlraum* radiation temperature profile shown in Fig. 2(a) and multigroup radiation diffusion, reproduce the foil trajectory very well, as shown in Fig. 2(b). From the simulations we then generate the acceleration profile at the embedded interface, $g(t)$, also shown in Fig. 2(b). The combination of layered target and shaped drive lead to multiple shock reverberations and hence substantial variations in $g(t)$. We calculate the linear regime RT growth factor by numerically solving the equation,

$$\partial^2 \eta(t)/\partial t^2 = \gamma^2 \eta(t), \tag{1}$$

where $\eta(t)$ is the time-dependent spatial amplitude of the perturbation. We assume an RT growth rate γ given by

$$\gamma^2 = [Akg/(1 + kL)] f_c, \tag{2}$$

where $A = (\rho_1 - \rho_2)/(\rho_1 + \rho_2)$ is the Atwood number ($\rho_2 < \rho_1$), $k = 2\pi/\lambda$ is the perturbation wave number, g is the acceleration of the interface, and $L = \rho/\nabla\rho$ is the density gradient scale length. The correction factor f_c is due to the finite thickness of the Ti foil [10, 14], and can be written in the form

$$f_c = (1 + r)/[1 + r \coth(kh)], \tag{3}$$

where $r = \rho_2/\rho_1$ is the ratio of fluid densities, and h is the layer thickness of the Ti foil. Note that Eqs. (2) and (3) reduce to the correct limiting form: as $h \to \infty$ and $L \to 0$, then $f_c \to 1$ and $\gamma^2 \to Akg$. All of the parameters for Eqs. (2) and (3) are time dependent, and taken from the 1D simulations. In the limiting case that all parameters are constant, Eq. (1) has the trivial RT solution $\eta = \eta_0 \exp(\int \gamma\, dt)$. Also, if the acceleration is zero, then $\gamma^2 = 0$ and Eq. (1) becomes $\partial\eta(t)/\partial t =$ const, which is the RM solution. We have tested our numerical algorithm against both of these limiting cases. Hence our numerical solution of Eqs. (1)–(3) incorporates seamlessly the growth from both the RM phase due to shocks traversing the interface and the later time exponential growth exhibited by the RT instability. The results of these calculations are shown by the smooth curves in Fig. 4(a), normalized to the data at $t = 2.7$ ns. We see that the RT growth at this compressible but embedded interface is reproduced reasonably well by this simple linear regime calculation. The divergence of the data from the calculations late in time is due to the onset of nonlinear behavior characterized by the formation of the spike and bubble structure.

To calculate the ablation-front growth, we use a modified Takabe approach, namely, we approximate the growth rate in the RT phase as

$$\gamma = [kg/(1 + kL)]^{1/2} - \beta k v_a. \tag{4}$$

Here k, g, and L are defined as above, β is an adjustable parameter, and $v_a = (dm/dt)/\rho_{\max}$ is the ablation velocity, where m corresponds to foil mass per unit area, and $\rho_{\max}$ is the maximum density at the ablation front. The correction for the finite layer thickness [Eq. (3)] is small for the thicker ablation-front foils and is neglected. Since the acceleration profile at the ablation front of the single-layer CH(Br) target is considerably smoother than that in the multilayer embedded interface target we may use the Wentzel-Kramers-Brillouin description of the evolution of the RT instability and start the growth factor calculation at shock breakout. Following the analysis in Ref. [8] we write

$$\text{growth factor} = \exp\left(\int \gamma\, dt\right), \tag{5}$$

where $\int \gamma\, dt$ represents the classical RT e-foldings after shock breakout. As before, the time-dependent values of all the parameters in Eq. (4) are taken from the 1D hydrodynamics simulation. We compare the calculated

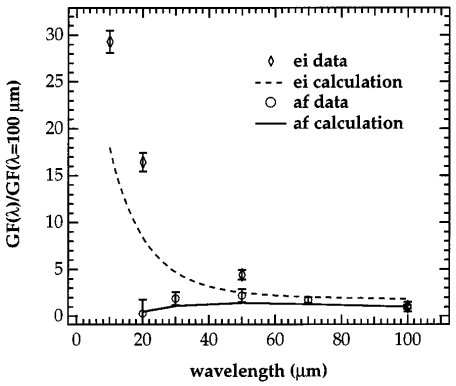

FIG. 5. Ratios of growth factor at 3.4 ns at the various wavelengths vs growth factor at $\lambda = 100$ μm for the embedded interface and ablation front. The smooth curves are generated from the calculations shown in Fig. 4.

growth with the observed growth after shock breakout ($t > 2.7$ ns), as shown by the smooth curves in Fig. 4(b), again normalized to the data at 2.7 ns. Using a value of $\beta = 3$, this simple model does a reasonable job of reproducing the data. The higher value of β used here compared to Ref. [8] compensates for the lower ablation velocity with a Planckian source lacking hard x rays in the drive.

To make the direct experimental comparison of ablation-front RT growth versus that at the embedded interface, we use ratios. In Fig. 5 we show for $t = 3.4$ ns the ratio of growth factor at each wavelength studied to that at $\lambda = 100$ μm. For the ablation-front case, we have added values at $\lambda = 30$, 70, and 100 μm from a previous investigation using the same drive but a different diagnostic [11]. The smooth curves represent the corresponding ratios from the calculations described above. The difference in the behavior of this ratio between the embedded interface and the ablation front is indeed striking. For the embedded interface, the growth of the shortest wavelength perturbations, $\lambda = 10$–20 μm, greatly exceeds the growth of the $\lambda = 100$ μm perturbation, in qualitative agreement with the classical linear analysis. (The underprediction of our classical simulation for $\lambda = 10$ and 20 μm may be the result of our approximation of the drive as Planckian, which delays the arrival of the first shock at the interface.) In marked contrast, at the ablation front, the growth at $\lambda = 20$ μm is strongly stabilized, as predicted by the Takabe analysis. This striking difference results from the large ablation velocity in indirect drive and the density gradient scale length at the ablation front. For the ~200 eV x-ray drive used [see Fig. 2(a)], growth of perturbations with wavelengths shorter than about 30 μm is strongly inhibited at the ablation front, whereas at the embedded interface these short wavelength modes grow the most. Figure 5 represents an unambiguous direct experimental demonstration of the stabilizing effect on RT growth of short wavelength perturbations at an ablation front as well as a measurement of the dispersion curve for RT growth at an embedded interface in a compressible medium.

The authors acknowledge fruitful discussions with T. S. Perry, the target fabrication efforts of H. Louis, T. Demiris, and R. Wallace, the expert technical assistance of S. Alvarez, A. Nikitin, and R. Mazuch, and the staff at Nova. This work was performed under the auspices of the U.S. Department of Energy by the Lawrence Livermore National Laboratory under Contract No. W-7405-ENG-48.

*Current address: Harvey Mudd College, Claremont, CA 91711.

[1] S. Chandrasekhar, *Hydrodynamic and Hydromagnetic Stability* (Oxford University Press, London, 1968).
[2] R. D. Richtmyer, Commun. Pure Appl. Math. **XIII**, 297 (1960); E. E. Meshkov, Sov. Fluid Dyn. **4**, 101 (1969).
[3] E. Muller, B. Fryxell, and D. Arnett, Astron. Astrophys. **251**, 505 (1991); M. Herant and S. E. Woosley, Astrophys. J. **425**, 814 (1994).
[4] J. D. Lindl and W. C. Mead, Phys. Rev. Lett. **34**, 1273 (1975); S. W. Haan, Phys. Rev. A **39**, 5812 (1989); C. P. Verdon *et al.*, Phys. Fluids **25**, 1653 (1982); S. E. Bodner, Phys. Rev. Lett. **33**, 761 (1974); J. Lindl, Phys. Plasmas **2**, 3933 (1995).
[5] H. Takabe *et al.*, Phys. Fluids **26**, 2299 (1983); M. Tabak *et al.*, Phys. Fluids B **2**, 1007 (1990).
[6] M. M. Marinak *et al.*, Phys. Plasmas (to be published).
[7] K. O. Mikaelian, Report No. UCID-19895, 1983; H. J. Kull, Phys. Rep. **206**, 197 (1991), and references therein; R. Betti *et al.*, Phys. Plasmas **2**, 3844 (1995); M. Emery *et al.*, Phys. Rev. Lett. **57**, 703 (1986); A. Caruso and V. A. Pais, Laser Part. Beams **12**, 343 (1994).
[8] S. V. Weber *et al.*, Phys. Plasmas **1**, 3652 (1994).
[9] J. Grun *et al.*, Phys. Rev. Lett. **58**, 2672 (1987); M. Desselberger *et al.*, Phys. Fluids B **5**, 896 (1993); S. G. Glendinning *et al.*, Phys. Rev. Lett. **69**, 1201 (1992).
[10] B. A. Remington *et al.*, Phys. Fluids B **4**, 967 (1992).
[11] B. A. Remington *et al.*, Phys. Plasmas **2**, 241 (1995).
[12] K. S. Budil *et al.*, Rev. Sci. Instrum. **67**, 485 (1996).
[13] J. T. Larsen and S. M. Lane, J. Quant. Spectrosc. Radiat. Transfer **51**, 179 (1994).
[14] L. D. Landau and E. M. Lifshitz, *Fluid Mechanics* (Pergamon, New York, 1987), p. 36, Sec. 12, prob. 3.